Aerial Manipulation via Modular Quadrotors with Passively Foldable Airframes

Huaiyuan Jia, Songnan Bai, and Pakpong Chirarattananon, *Member, IEEE*

***Abstract*—The need for physical interactions and aerial manipulation has driven the demand for small multirotor vehicles with higher degrees of actuation and adaptability. This leads to the development of reconfigurable flying robots and modular flight platforms. In this work, we propose a modular vehicle comprising flight-capable quadrotors with passively deformable rotor arms as subunits. The foldable arms with preloaded elastic components are designed to be stable in both folded and unfolded states such that the reconfiguration can be achieved passively through the manipulation of the propelling thrust. A docking mechanism is devised to permit multiple modules to combine during a mission without human intervention. Through a series of experiments, we show that passive reconfigurability enables the platform to perform perching. With the added modularity, the integrated platform can be used to perform thrust vectoring or grip and transport heavier payloads. The ability to accomplish a wide range of tasks in a single platform is unique from existing aerial robots, thanks to the combination of reconfigurability and modularity.**

I. Introduction

To date, micro aerial vehicles have been increasingly deployed for various applications such as inspection, exploration, and agriculture. However, early real-world usage of such robots are still predominantly limited to tasks that do not require the vehicles to interact directly with environments. The potential to conduct manipulation tasks while flying has further driven the developments of small flight platforms [1]–[4]. While pragmatic, a direct incorporation of tools such as a motorized gimbal stabilizer or a robotic arm as a payload results in the added weight [5], severely reducing the flight endurance. As an alternative solution, fully actuated vehicles featuring six and more rigidly fixed rotors in non-planar configurations have been pioneered [6]–[9]. Nevertheless, such platforms also undesirably suffer from the thrust loss caused by unaligned rotors.

Small rotorcraft can improve their functions and flexibility by adapting their morphology and modularity. Quadrotors can control their wrench with parallel rotors by using servomotors to tilt them or deform the airframe [10]–[13]. Depending on the design, active (actuated) [11]–[14] and passive [15]–[17] reconfigurations enable aerial robots to use their structural components to grasp an object [12], [13], [16], perch [14], [16], or shrink its body to negotiate narrow gaps [15], [16]. Among these, the active implementation gains advantages from more precise and controllable deformation with the ability to perform the transformation on demand. With minimal added weight and power, the passive method relies on interactions with the environment [17] or operational conditions [15], [16] to achieve the deformation. For instance, in [15], [16], the airframe reconfiguration is directly coupled with the propelling thrust. As a consequence, the rotor arms are only folded at low motor commands. The thrust reduction limits the mass of the payload carried by the folded rotor arms of a 624-g robot to only 83 g [16].

Similarly, modular designs allow aerial robots to realize vehicular configurations that are adaptable to various needs. For small flying robots, subunits of a final vehicle can be non-autonomous thrusters [10], [13], [18], [19] or flight-capable robots themselves [20]–[25]. By separating a conventional rotorcraft into individual thrust units, they can be flexibly affixed to different payloads for transport with the number of required modules depending on the mass and size of the payload [18], [19]. Modular vehicles constructed from flight-capable units similarly benefit from an adjustable configuration. When each subunit is capable of flying, it becomes possible for the platform to assemble or disassemble without manual human assistance [22], [25]. In both regimes, the degree of adaptability is largely pre-determined by the attachment mechanisms and control methods. When the rotor axes are required be aligned [18]–[20], [22], [25], after the construction, the resultant robots behave similarly to conventional rotorcraft. To make the platform fully actuated, nonidentical modules with different thrust alignments are introduced in [24]. Alternatively, servomotors are incorporated to allow the arrangement between modules to be varied after the platform has been constructed [13] so that thrust vectoring and body-based grasping can be achieved.

In this article, we propose a highly versatile modular flight platform that is composed of multiple flight-capable quadrotors with passively deformable airframes. As illustrated in Fig. 1A and Movie 1, as a module, each quadrotor embraces four symmetrically arranged revolute joints. When the propelling thrust is lowered, the preloaded elastic component induces the respective arm to fold down by 90°, allowing it to grasp an object or perform other aerial manipulation tasks. This is without carrying additional grippers or actuators. To combine multiple identical modules, the quadrotors are docked vertically. Aided by small neodymium magnets, the docking mechanisms precisely latch the robots together when they come in contact. In the situation where two modules are

This work was supported by the Shenzhen-Hong Kong-Macau Science & Technology Project (Category C) (contract number SGDX20220530111401009) and the Research Grants Council of the Hong Kong Special Administrative Region of China (grant number CityU 11205419).

H.J., S.B., and P.C. are with the Department of Biomedical Engineering, City University of Hong Kong, Hong Kong SAR, China (emails: hhjia2-c@my.cityu.edu.hk, pakpong.c@cityu.edu.hk).

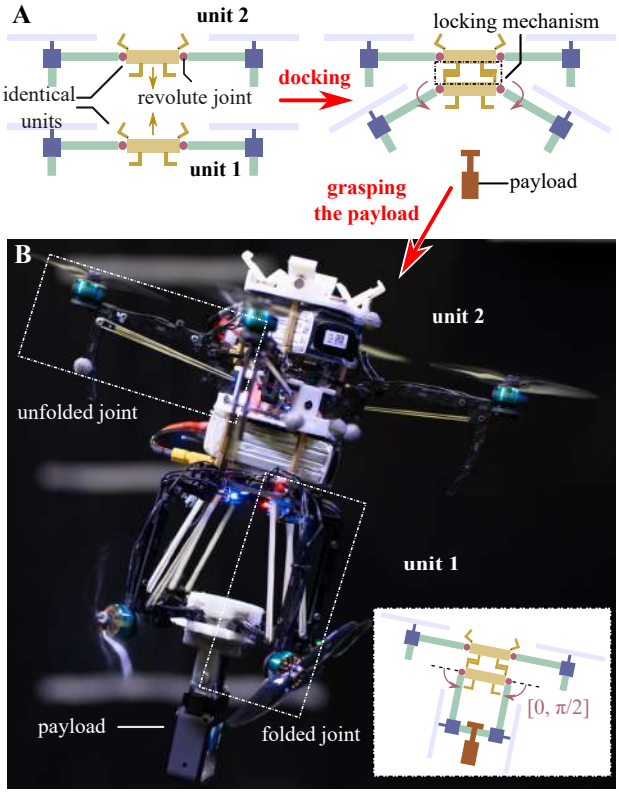

Fig. 1. (A) Illustration of the modular and reconfigurable flight platform. Two flight-capable units are docked with the lower unit grasping a payload using its passively foldable rotor arms. (B) Photo of a robot constructed from two flight modules carrying a small camera as payload. The folded arms on the lower flight unit produce the horizontal thrust component to keep the robot tilted while hovering in place.

integrated (Fig. 1B), the lower unit with folded propellers can hold a light object while simultaneously producing a horizontal thrust component. If required, an additional module can be rapidly stacked on top to accommodate a heavier payload. The ability to easily increase the number of units in the middle of an operation and passively tilt the rotors makes the platform unique and suitable for a wide range of aerial manipulation tasks. The combination of the airframe reconfigurability and quick module assembly permits the platform to perch on a narrow structure, grip an object, carry a heavy payload or change the overall thrust vector direction.

To accomplish several aerial manipulation tasks, the design of the platform differs from previous aerial vehicles in three main aspects.

(i) Compared to non-modular servo-actuated deformable rotorcraft [11], [12], [14], the foldable rotor arms in this work are passive. Yet our platform can perform thrust vectoring and carry a heavy payload (1.4 kg; four times the weight of a single module or 1.33 times of the 3-module platform). This is by using a folded airframe as grippers and leveraging additional rotors incorporated via the modular design.

(ii) Compared to previous modular systems with no inter-module actuators [18]–[20], [22], [24], [25], the foldable airframes herein permit the system to reconfigure after it has been constructed and deployed for flight, rendering it more adaptable to operational requirements such as perching, thrust vectoring, or payload transport. Compared to modular systems with inter-module actuators for in-flight reconfiguration and aerial manipulation [10], [13], the proposed system has passive joints. This eliminates the added mass and power consumption of extra actuators while still enabling reconfiguration after deployment for enhanced adaptability.

(iii) Existing modular systems capable of aerial manipulation, such as the multi-link DRAGON robot [13] and the robot made of double-gimbal thrust modules [10], cannot rapidly add or remove modules after construction. This is because each subunit is not flight-capable. The flight ability of each subunit enables an unassisted assembly to meet increased operational demands. Adaptability is advantageous for payload transport, for example.

All in all, through passive reconfigurability and modularity, we achieve perching, grasping, adaptively load carrying, and thrust vectoring capabilities in a single platform, which is unique from existing aerial robots as highlighted in Supplementary Table S1. In the next section, we present the platform design and the prototype of flight units. This is followed by the descriptions of the foldable airframes and docking mechanisms. Section III provides details of the flight dynamics and the implementation of the flight controller of the modular system, taking into consideration the reconfigurability. Three aerial manipulation experiments are reported in Section IV to thoroughly demonstrate the advantages of the modular and deformable platform. Lastly, a brief conclusion is given in Section V.

II. Reconfigurable and Modular Design

A. Design Overview and Working Principles

Our proposed platform design uses passive reconfigurability and modularity to enhance the system's capabilities for various tasks, especially when multiple quadcopter units are combined. For each flight-capable unit, the reconfigurable airframe enables an individual robot to grab an object or perch on a narrow structure when it is not flying. Moreover, when multiple modules are combined, the integrated robot with several propellers pointing in different directions gains additional degrees of control outputs, with the possibility of being fully actuated or gripping and carrying a heavy payload.

As depicted in Fig. 1A, each quadcopter unit resembles a conventional vehicle. The difference lies in the passively reconfigurable joints adopted at each propelling arm, allowing not only each thrust vector to re-orient by 90° but also the arms to act as grippers. The elastic element incorporated into these joints means the arms fold by default and unfold when thrust exceeds a threshold. In addition, locking mechanisms enable multiple units to dock together. The strategy enables the robots to transform without the need for extra actuators.

B. Prototypes and Components

A subunit robot is shown in Fig. 2A. The central airframe of the prototype was manufactured from 3-mm-thick carbon fiber sheets. The foldable arms are 2 mm thick and 90 mm long (l_a). The hook-shaped arm tips serve as landing gears or grippers, depending on the operational stage. Each robot includes four

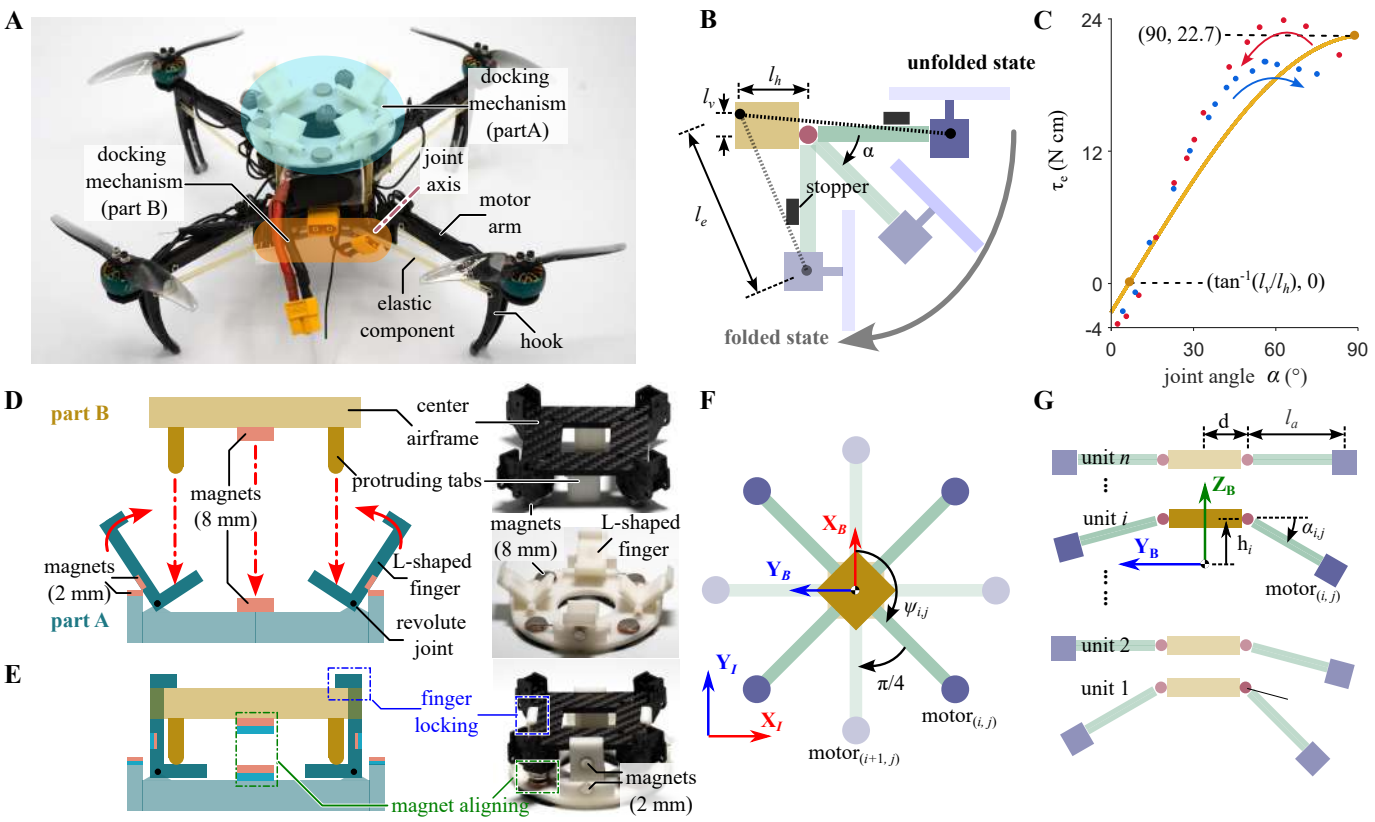

Fig. 2. (A) Prototype of a reconfigurable quadrotor module showing the foldable airframe and docking mechanism. (B) Schematic diagram of the passive revolute joint. (C) The restoring joint torque plotted against the joint angle. Measurement results are shown in points. (D) and (E) Diagram and photos illustrating the design of the two-part docking mechanism before (D) and after (E) docking. (F) Drawing of a multi-module system consisting quadrotor units docked together with yaw offsets (top view). (G) Diagram illustrating the robot's configuration when multiple units are vertically stacked.

brushless motors (3750-KV) with 4-inch 2-blade propellers and is controlled through a programmable flight control board (Bitcraze, Crazyflie Bolt). They are powered by a 1300-mAh 4S battery and a 4-in-1 electronic speed controller (LANRC, UFOFPV BLS 45A). The total mass of one module is 350 g. Using the setup in [26], the maximum thrust generated by one robot was found to be 21.2 N (2.16 kg).

C. Reconfigurable Airframe

Each flight unit features four passive revolute joints that connect the rotor arms to the airframe. As shown in Fig. 2A, four rotational joints with axes perpendicular to the axial arm directions and propelling axes are arranged symmetrically. Each joint is mechanically limited to rotate by 90° between the flight and folded (downward) configurations. The joint design and working principles are based on the passive mechanism presented in our previous work involving a smaller aerial vehicle that exploits the reconfiguration to roll on the ground as a secondary mode of locomotion [15]. Herein we provide a brief description for completeness and point out some differences. As illustrated in Fig. 2B and G, each joint features a link of length l_a connecting to the central airframe (mechanical ground) with a stretched elastic element of length l_e. The length l_e is determined by the joint angle α (defined as 0° and 90° when the joint is fully unfolded and folded, respectively) according to a geometric relationship.

$$l_e = \sqrt{(l_a \cos\alpha + l_h)^2 + (l_a \sin\alpha + l_v)^2}, \tag{1}$$

where l_h and l_v are horizontal and vertical offsets (see Fig. 2B). As a result, the elastic tension, approximately proportional to an extension of l_e from the nominal length l_0 through a stiffness k_e, depends on the joint angle α as $f_e = -k_e(l_e - l_0)$. It follows that the restoring torque is a function of the joint angle α according to

$$\tau_e = k_e(l_a/l_e)\,(l_h \sin\alpha - l_v \cos\alpha)\,(l_e - l_0)\,. \tag{2}$$

Depending on the design parameters, the resultant torque profile can be manipulated. For the prototype shown in Fig. 2A with the chosen link length of l_a=9 cm, we opted for k_e, l_0, l_h, and l_v as listed in Table I. The vertical offset distance l_v is particularly important as it dictates the torque characteristic in the unfolded state. Unlike our previous implementation, in which l_v was zero, the positive distance here ensures that the torque is negative when α is near zero as plotted in Fig. 2C. As α increases, τ_e rises and the torque direction is reversed when $\alpha = \tan^{-1}(l_v/l_h)$. The increasing trend continues until α reaches 90° and the link is prevented from folding further by the stopper. With the resultant profile seen in Fig. 2C, both unfolded and folded arm configurations are stable when gravity is neglected. Nevertheless, since the negative torque in the unfolded state (≈ -2.6 Ncm) is only marginally greater than the positive torque produced by the weight of

TABLE I
PHYSICAL PARAMETERS

Var	Value	Unit	Var	Value	Unit
m	350	g	d	44	mm
l_v	2	mm	l_h	18	mm
l_0	18	mm	l_a	90	mm
k_e	196	N/m	α	[0,90]	deg
τ_e	[-2.6,22.7]	Ncm			

the motor-propeller pair 25 g $\times$ 9 cm $=$ 2.3 Ncm, the robot relies on the propelling thrust to keep the arm unfolded when flying. The nominally negative torque inhibits the arm from folding accidentally in flight when the thrust is momentarily reduced. When the motor is powered off, small disturbances or vibration is sufficient to induce the arm to fold. When folded ($\alpha = 90^\circ$ in Fig. 2C), the relatively large positive torque (22.7 Ncm) keeps the arm folded even when the rotor is moderately actuated to produce thrust in the horizontal direction. In practice, the arm folding and unfolding actions are accomplished passively depending on the state of the propelling thrust.

We conducted measurements using a multi-axis force/torque sensor (ATI Nano 25) [26] to assess the validity of the torque equation (2). As shown in Figure 2C, the results confirmed the increasing trend in torque magnitude associated with joint angle. However, the measurements also revealed the presence of unmodeled hysteresis at large α, whereby the torque values differed depending on whether the joint angle was increasing or decreasing. This phenomenon is likely due to friction and possible viscoelasticity that is not captured by the model.

D. Docking Method and Mechanism

As multiple flight units are combined as a single vehicle, the added propellers improve the payload capacity and/or the degree of actuation. This is realized by the docking mechanisms that let robots attach to one another along their vertical axis (Z_B).

To facilitate the attachment, each robot is equipped with a two-part mechanism (parts A and B) affixed on top and below the flight unit, such that the piece on top of one robot can easily *snap on* to the matching piece at the bottom of another robot as captured by Fig. 1B. Two key specifications are considered in the design of the attachment mechanism: tolerance against small misalignments and robustness against an accidental release.

The mechanism contains four pairs of small neodymium magnets (8 mm diameter) placed symmetrically around its perimeter. The magnetic attraction between Parts A and B is sufficient to overcome small translational and yaw misalignments between the upper and lower robot units during docking. Simultaneously, Part B has four protruding tabs situated symmetrically between its magnets. These tabs engage with four L-shaped, hinged fingers on Part A (Fig. 2D and E). Prior to docking, the fingers are held open by smaller magnets (2 mm diameter). As the tabs slide into the fingers during docking, they overpower the magnetic force and cause the fingers to rotate and lock onto the tabs. This secures the upper robot to the lower one, preventing release under acceleration or deceleration until the fingers are manually disengaged.

The mechanisms were printed with PLA and 304 stainless steel rods (1 mm in diameter) were adopted as the hinge axles for the pivoting fingers. The mechanisms are arranged such that the propeller arms of stacked robots are diagonal (Fig. 2F). In this pattern, the wake interaction is minimized, and propeller arms cannot collide when one is accidentally folded. The diagonal arrangement allows robots to be stacked closely, rendering the entire system more compact.

Drop tests were conducted to evaluate the docking reliability (see Supplementary Materials). The tests assessed the effects of position and angular misalignments on docking success. The results show that the docking mechanism achieves a 100% success rate for small misalignments (displacement lower than 2 cm or yaw error below 25°).

III. DYNAMIC MODELING AND CONTROL

In this section, we inspect the dynamics of the robot when multiple robots are combined. The degree of actuation varies depending on the number of robots and joint configurations. The flight dynamics are first analyzed, followed by the controller design.

A. Coordinates and Control Inputs

Assuming the system is composed of n subunits as shown in Fig. 2F and G, the body-fixed frame is located at the center of mass (CoM) of the entire system. The modules are indexed by 1 to n from bottom to top. We adopt the notation $(\cdot)_{i,j}$ with $i \in \{1, 2, ..., n\}$ and $j \in \{1, 2, 3, 4\}$ to label the j^{th} propeller of the i^{th} module, such that $\psi_{i,j}$ denotes the relative yaw angle of the j^{th} arm of module i, and angle $\alpha_{i,j} \in [0, 90^\circ]$ is the joint angle of the respective rotor arm.

To determine the total force produced, we begin with an individual thrust vector (with respect to the body frame):

$$\boldsymbol{T}_{i,j} = T_{i,j}\boldsymbol{e}_{i,j}, \tag{3}$$

where $\boldsymbol{e}_{i,j} = [\sin\alpha_{i,j}\cos\psi_{i,j}, \sin\alpha_{i,j}\sin\psi_{i,j}, \cos\alpha_{i,j}]^T$ is a unit directional vector associated with propeller i, j. In the case that the arm is fully unfolded $\alpha_{i,j} = 0$, $\boldsymbol{e}_{i,j}^T$ reduces to $[0, 0, 1]^T$. From here, we obtain the vector of total thrust by separating the direction and magnitude terms:

$$\sum_{i,j} \boldsymbol{T}_{i,j} = \boldsymbol{A}_{3\times 4n}\boldsymbol{T}_{4n\times 1}, \tag{4}$$

with the mixing matrix $\boldsymbol{A} = [\boldsymbol{e}_{1,1}, \boldsymbol{e}_{1,2}, ..., \boldsymbol{e}_{n,4}]$ and input vector $\boldsymbol{T} = [T_{1,1}, ..., T_{n,4}]^T$.

The torque produced by the propellers is attributed to the induced drag and thrust. The drag, parallel to the propeller axis, is characterized by the torque-to-thrust ratio $k_{i,j}$ (positive or negative). The thrust-related element is dependent on the force position with respect to the CoM, we define $\boldsymbol{r}_{i,j}$ as the position vector of a particular propeller. The radial distance of the respective propeller from the vertical axis (Z_B) is the sum of a fixed length d and the projected length of the folding section of the propeller arm $l_a\cos\alpha_{i,j}$ (see Fig. 2G). Along the Z_B axis, the vertical displacement is $h_i - l_a\sin\alpha_{i,j}$ when

h_i is the vertical distance from the CoM of module i to the CoM of the robot. Together, we obtain

$$\boldsymbol{r}_{i,j} = \begin{bmatrix} (d + l_a \cos\alpha_{i,j}) \cos\psi_{i,j} \\ (d + l_a \cos\alpha_{i,j}) \sin\psi_{i,j} \\ h_i - l_a \sin\alpha_{i,j} \end{bmatrix}. \tag{5}$$

Therefore, the total propelling torque is

$$\sum_{i,j} \boldsymbol{\tau}_{i,j} = \boldsymbol{B}_{3\times 4n} \boldsymbol{T}_{4n\times 1}, \tag{6}$$

in which each column of the mixing matrix $\boldsymbol{B}_{3\times 4n}$ is a combination of two contributing factors: $k_{i,j}\boldsymbol{e}_{i,j} + \boldsymbol{r}_{i,j} \times \boldsymbol{e}_{i,j}$.

As a result, (4) and (6) provide the body-centric thrust and torque vectors of the n-module system as a linear combination of individual thrust amplitudes $T_{i,j}$. Both quantities depend on the current joint configurations, which are assumed known by the flight controller.

B. Flight Dynamics and Controller Design

Similar to a regular rotorcraft, the robot is regarded as a rigid body as the reconfiguration only occurs between flights. The translational dynamics of the robot are, therefore, [27]

$$m\ddot{\boldsymbol{x}} = -mg\boldsymbol{e_3} + \boldsymbol{RAT}, \tag{7}$$

where mg is the weight of the system, $\boldsymbol{e}_3 = [0, 0, 1]^T$ is a basis vector, and $\boldsymbol{R}$ is a rotation matrix associated with the body frame. The time evolution of $\boldsymbol{R}$ is dictated by the body-centric angular velocity $\boldsymbol{\Omega}$. The angular acceleration is described by Euler's rotation equations

$$\boldsymbol{J}\dot{\boldsymbol{\Omega}} + \boldsymbol{\Omega} \times (\boldsymbol{J}\boldsymbol{\Omega}) = \boldsymbol{BT}. \tag{8}$$

With the dynamics of the n-unit multirotor derived above, we can design the control scheme to control the n-unit system taking into account the rank condition of $\boldsymbol{A}$ in (7).

1) Control Strategy: The control of an n-unit vehicle is dependent on the robot configuration or, mathematically, the rank of $\boldsymbol{A}$. In this work, we limit the scope two scenarios: rank$(\boldsymbol{A}) = 1$ and rank$(\boldsymbol{A}) = 3$. The former case corresponds to a robot with no folded rotor arms and the robot behaves identically to a conventional multirotor vehicle. The latter case occurs when at least all four arms on one flight modules are folded, making the robot fully actuated. This includes when the robot transport a payload as seen in Fig. 1.

When rank$(\boldsymbol{A}) = 1$, flight controllers previously developed can be readily implemented. Similar to our previous work [15], the cascaded controller from [28] is adopted. On the other hand, when the robot is fully actuated, position and attitude can be simultaneously commanded. However, some care should be taken on the rotors' thrust limit. Below, the framework for stabilizing the system with rank$(\boldsymbol{A}) = 3$ is explained.

2) Attitude and position commands: Since the translational dynamics of the fully-actuated robot in (7) is second order, the robot stabilizes to the desired trajectory $\boldsymbol{x}_d$ when the input $\boldsymbol{RAT} = \boldsymbol{u}_p$ with

$$\begin{aligned} \boldsymbol{u_p} =& m\ddot{\boldsymbol{x}}_d + mg\boldsymbol{e_3} - \boldsymbol{K}_d(\dot{\boldsymbol{x}} - \dot{\boldsymbol{x}}_d) \\ & - \boldsymbol{K}_p(\boldsymbol{x} - \boldsymbol{x}_d) - \boldsymbol{K}_i \int (\boldsymbol{x} - \boldsymbol{x}_d)\,\mathrm{d}t, \end{aligned} \tag{9}$$

where $\boldsymbol{K}_{(.)}$'s are positive definite gain matrices. The integral term in (9) drives the position error to zero over time, even with imprecise model parameters or payload-induced imbalance. Similarly, according to [9], the attitude of the robot from (8) stabilizes to the attitude setpoints $\boldsymbol{R}_d$ when the input $\boldsymbol{BT} = \boldsymbol{u}_a$ with

$$\boldsymbol{u}_a = \boldsymbol{\Omega} \times (\boldsymbol{I}\boldsymbol{\Omega}) - \boldsymbol{K}_R(\boldsymbol{R}_d^T\boldsymbol{R} - \boldsymbol{R}^T\boldsymbol{R}_d)^\vee - \boldsymbol{K}_\Omega\boldsymbol{\Omega}, \tag{10}$$

where $\boldsymbol{K}_R$ and $\boldsymbol{K}_\Omega$ are positive definite gain matrices and $^\vee : SO(3) \to \mathbb{R}^3$ is the inverse of the hat map.

In the next step, the thrust commands $\boldsymbol{T}$ is computed from $\boldsymbol{u}_p$ and $\boldsymbol{u}_a$, taking into account the limits of $T_{i,j}$.

3) Thrust and limits: Combining (9) and (10), we yield

$$\begin{bmatrix} \boldsymbol{R}^T\boldsymbol{u}_p \\ \boldsymbol{u}_a \end{bmatrix} = \boldsymbol{CT}, \tag{11}$$

where $\boldsymbol{C} = [\boldsymbol{A}^T, \boldsymbol{B}^T]^T$ is a $6\times 4n$ matrix. For a fully actuated robot with rank$(\boldsymbol{A}) = 3$ and $n \geq 2$, rank$(\boldsymbol{C}) = 6$. This means (11) is under-determined and there are infinitely many $\boldsymbol{T}$ solutions that satisfy (11). They are all given by

$$\boldsymbol{T} = \boldsymbol{C}^+ \begin{bmatrix} \boldsymbol{R}^T\boldsymbol{u}_p \\ \boldsymbol{u}_a \end{bmatrix} + (\boldsymbol{I} - \boldsymbol{C}^+\boldsymbol{C})\boldsymbol{\zeta}, \tag{12}$$

for arbitrary vector $\boldsymbol{\zeta}$. This is because $\boldsymbol{C}(\boldsymbol{I} - \boldsymbol{C}^+\boldsymbol{C}) = \boldsymbol{0}$. The method to obtain $\boldsymbol{T}$ with non-negative elements (as thrust values can only be positive) have been discussed in [8], [29]. When rank$(\boldsymbol{C}) = 6 < 4n$, $(\boldsymbol{I} - \boldsymbol{C}^+\boldsymbol{C})$ is a non-zero matrix and $\boldsymbol{\zeta}$ can be chosen to ensure that all elements of $\boldsymbol{T}$ are non-negative. Without $\boldsymbol{\zeta}$, it is likely that some thrust commands belonging to folded propellers become negative when the robot needs to generate a horizontal thrust component.

However, the solution provided by (11) cannot impose an upper limit on $T_{i,j}$. When a large command is sent to a folded propeller, it may unintentionally unfold. To prevent this, we saturate thrust commands for folded propellers. Since the elastic torque when the joint angle $\alpha = 90°$ is 22.7 Ncm (refer to Fig. 2C), the ideal thrust limit for $l_a = 9$ cm is 2.5 N. Hence, the thrust limit for folded rotors is set to 2.2 N, slightly lower than the ideal limit. This constraint could prevent the robot from realizing trajectories that require substantial acceleration along the horizontal body direction. This can be avoided in the trajectory planning process as discussed in [6].

IV. Experimental Demonstrations

We conducted three sets of experiments to show the advantages of modular and reconfigurable quadcopters. First, a single robot demonstrated the use of the passively reconfigurable airframe as grippers for perching on a structure. The second demonstration involved two robots integrated as a fully-actuated vehicle, hovering in place while tilting a camera phone up and down. Finally, three flight modules were used to carry a payload too heavy for a single or two flight units.

A. Flight Setup and Controller Implementation

Experiments were carried out in a $2.5 \times 2.5 \times 2$-m flight arena. Motion capture cameras were used to provide position feedback for control purposes. The onboard IMUs were

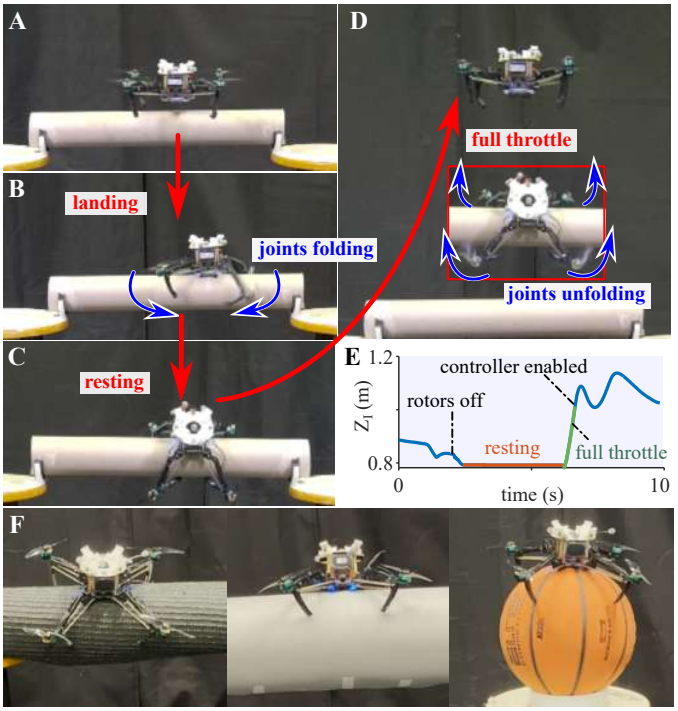

Fig. 3. Perching and take-off experiment. (A) A quadrotor wih foldable airframe approaches the target structure (paper tube, radius: 5 cm). (B) The robot switches off the propellers, triggering the arm folding for perching. (C) The robot stays anchored on the rod in an unpowered mode. (D) The vehicle unfolds the rotor arms through the propulsion and simultaneously takes off. The flight controller is activated shortly after the robot is clear from the structure. (F) The robot perching on objects of different sizes (radius: 7, 8, and 12 cm) and surfaces.

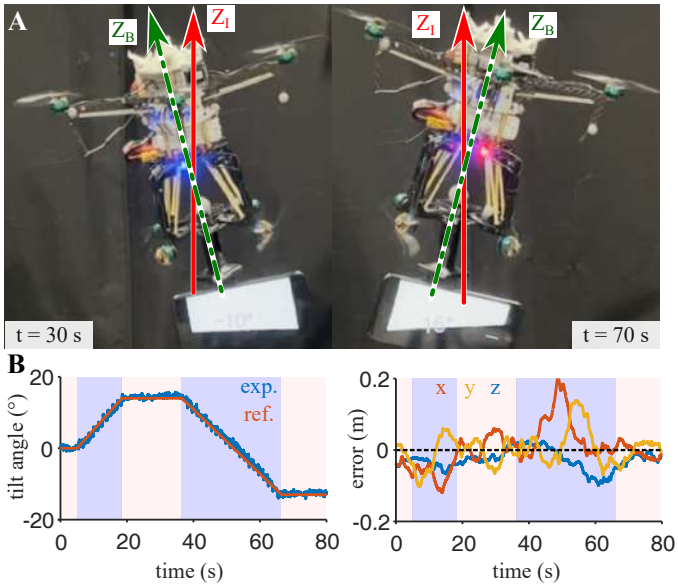

Fig. 4. (A) Photos of the two-module robot carrying a cell phone and hovering in place at varying pitch angles (left: starting angle of 14°; right: final angle of -14°). (B) Plot of the pitch angle when the robot was hovering and position of the robot over time. The RMSEs of the tilt angle and position tracking are $1.0°$ and $[6, 5, 4]$ cm.

adopted to provide information to the attitude controller. A ground station computer transmitted the data (including the position controller output, model parameters, and the desired attitude) to quadrotor modules via radio communication. In the experiments, we assumed the knowledge of the state of the propeller arms as either fully folded ($\alpha = 90°$) or unfolded ($\alpha = 0°$). This is needed as the current prototypes do not yet include sensors for detecting the joint angles autonomously.

When multiple modules formed a single vehicle, the exact configuration of the entire robot was assumed known by each module. That is, the thrust/torque mapping and distance parameters (e.g. h_i and $\psi_{i,j}$) were available to all modules. To control the combined robot, the same controller designed for the respective vehicle's configuration) was implemented. Nevertheless, each module relied on its own IMU measurements and only the four thrust commands corresponding to each respective module were routed to their motors. During the experiments, the reference trajectories (position and attitude) were pre-planned and a human pilot remotely triggered the switches between different flight segments or experimental stages. Manual planning and switching were required as the robot was not equipped with visual-inertia navigation ability and could not directly sense the surroundings (such as autonomously identifying the perching location).

B. Perching and Take-off by Reconfigurable Airframe

This experiment shows that, despite having no additional actuators, a single robot is able to grab onto a narrow structure to conserve energy before continuing flying afterward. As captured in Fig. 3 and Movie 1, a cylindrical tube (with a diameter of 10 cm) was adopted for perching. In flight, the robot was commanded to hover above the structure, leaving a gap of $\approx$ 5 cm in between. Thereafter, the propelling commands were ramped down to zero instantly when it is deemed safe by the pilot. Following a brief drop, the impact with the structure triggered the mildly bi-stable arms to fold. The robot firmly held onto the structure, making use of the hooks at the tips of the propelling arms, and entered the resting state with low power consumption.

To take off, the robot first applied full throttle to quickly unfold the arms and lift off in open-loop (Fig. 3D). After 0.5 s, when the robot was far enough from the structure (the gap was $\approx$ 20 cm), the flight controller was activated to modulate the propelling thrust and stabilize the robot for flight. The perching demo here verified that the bi-stable reconfigurable airframe functions as intended despite having no active control. The grasping force generated was sufficient to stabilize the robot on a narrow (10 cm) non-flat surface. Further experiments (Fig. 3F and Supplementary Figure S6) show the robot can stably perch on cylindrical and spherical objects with radii of 7, 8, and 12 cm, but it flipped upside-down when the object is too narrow (radius of 2 cm).

C. Aerial Manipulation with a Fully Actuated Two-Unit Robot

Here, two flight units are combined to create a fully-actuated vehicle that is able to tilt a mobile phone (payload) up and down via a pitching motion while keeping the robot's position

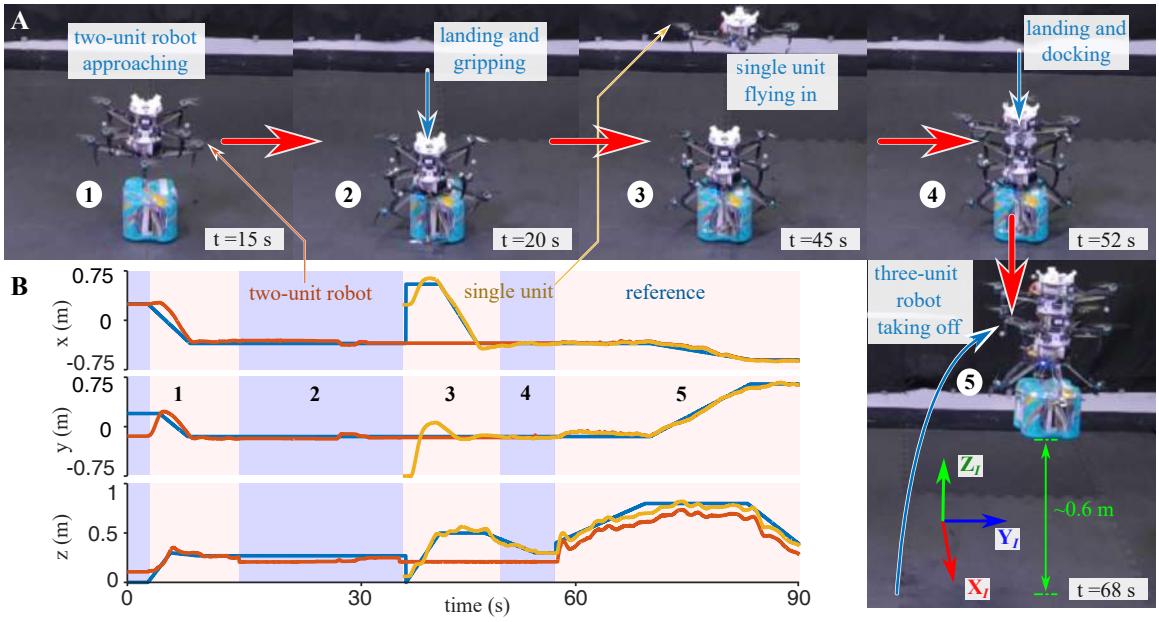

Fig. 5. The experiment of carrying a 1.4-kg payload can be divided into five stages. ① Two-module robot approaching the payload; ② The robot passively grasps the payload using the rotor arms of the bottom unit after landing but fails to lift the payload (total weight of the system (2.1 kg) similar with the thrust capacity of the upper unit (21 N)); ③ Another flight module maneuvers in; ④ The single module lands, and docks on the two-unit robot; ⑤ The three-unit vehicle successfully takes off with the payload thanks to the combined thrust generated by the two upper flight modules. (A) Sequential images and (B) the position tracking performance of the experiment. The transition between stages is remotely triggered by the pilot. The RMSEs ($60 \text{ s} < t < 90 \text{ s}$) for position along the three axes were 5 cm, 6 cm, and 10 cm.

stationary. As shown in Figs. 1 and 4, we formed a robot from two flight modules, with the lower module carrying a cell phone with a holder (250 g in total) using its four folded propelling arms. The center of the phone was horizontally offset from the robot's vertical axis by 2 cm to investigate the controller's ability to deal with an unmodeled imbalance. In this state, the robot was able to produce (limited) forces in the plane perpendicular to its vertical axis (Z_B), rendering it fully actuated. The maximally achievable tilt angle at hovering is restricted by the joint torque limit and dependent on the mass of the payload as discussed in the Supplementary Materials.

During the flight, the octa-rotor robot with a total weight of $2 \times 350 + 250 = 950$ g was initially commanded to hover 1.2 m above the ground with the pitch angle of $0°$.Then the pitch angle gradually increased to $14°$. In this state, two lower propellers each generated a thrust of 1.7 N on average in order to produce the combined horizontal force of 2.3 N to maintain the position. The 1.7-N thrust corresponds to the joint torque of 15 Ncm, safely below the 22.7-Ncm counter-torque limit provided by the elastic element τ_e (Fig. 2C). In other words, the pitch angle of $14°$ is near the practical limit imposed by the specs of the reconfigurable airframe.

After 20 s at a pitch angle of $14°$, the setpoint was steadily lowered to $-14°$ over 30 s. Position errors arose from imprecise model parameters and payload imbalance, but the integral term in the controller drove the errors to zero over time. For instance, position errors between t =40 s and 60 s diminished by t =65 s despite the maintained $-14°$ pitch angle. Disabling the integral term caused position RMSEs at least twice as large (see Figure S7). The integral action is crucial for achieving precise position control in the presence of persistent errors or disturbances. Overall, the flight results manifest the fully-actuated ability of the proposed modular aerial platform and the effectiveness of the integral term to deal with imprecise models and imbalanced payload.

D. Carrying a Heavy Payload with Three Flight Units

One advantage of the modular design is the capability to combine more units to accommodate an elevated requirement. In this example, we illustrate that when a 2-unit platform (700 g) was unable to lift a 1.4-kg payload (the maximum thrust of the upper unit is only 2100 g, similar to the total mass). Hence, another flight module could maneuver in to construct a 3-unit system (1050 g; with a combined thrust limit of 4200 g) on-the-fly to accomplish the transport task.

As detailed in Fig. 5 and Movie 1. The payload was a pack of four 335-ml beverage cans on the ground. To begin, the two-module robot was instructed to fly and land on top of the payload. The landing sequence, accomplished by turning off the propellers on the bottom unit, resulted in the grasping action (arm folding) similar to the perching procedure. During this, the propellers on the upper robot remained active to prevent the arms from folding unintentionally. After the hooks located at the end of the arms are anchored into the plastic packaging, resulting in an adequately stable grip (without anchoring, the payload capacity is dependent on the friction coefficient and severely limited to 400-500 g as detailed in the Supplementary Materials). The robot then attempted to take off by ramping up the propellers on the upper unit. However, the weight of the payload exceeded the thrust capacity of the two-module robot. To resolve this, the third flight unit flew in and slowly landed on top of the existing platform. The weight of the robot engaged the mechanism, and all three units were

docked together. With three modules, the thrust generated by the top two units was adequate for the 1050-g platform to lift off with the 1.4-kg payload as captured by Movie 1.

V. Conclusion

We have introduced a modular reconfigurable quadrotor platform that can achieve various aerial manipulation tasks. By adopting the passive joints, each flight module accomplishes the reconfiguration without extra actuators, preserving flight efficiency and payload budget. When integrated with the modular design, the system can be scaled up to accommodate heavier payloads or enhance the control degrees of freedom by leveraging airframe deformation. The integral term in the position controller can accommodate moderate changes in payload and modeling errors, but significant payload increases or modeling inaccuracies may exceed the controller's stability margins unless more robust control methods are adopted [30]. In flight experiments, we show that the platform can firmly clutch structures for landing or grip a heavy payload for transport, leveraging multiple units to satisfy different task requirements. This is unique from other existing robots that are capable of accomplishing these functions (such as perching or transporting a heavy payload) independently. The versatility of the proposed platform is a consequence of both reconfiguration and modularity. Nevertheless, the passive strategy renders arbitrary angular and torque control of the folding arms infeasible in this work.

In the future, we seek to include active joint angle sensing using Hall effect sensors. This would allow the robot to autonomously detect its current configuration for control purposes and to prevent collisions from accidental arm folding. Additionally, an improved attachment mechanism could allow undocking to be triggered on demand or in flight without human intervention. Such developments would increase the robot's autonomy and versatility.

References

[1] F. Ruggiero, V. Lippiello, and A. Ollero, "Aerial manipulation: A literature review," *IEEE Robotics and Automation Letters*, vol. 3, no. 3, pp. 1957–1964, 2018.

[2] P. H. M. Souza and K. Stol, "Constrained dynamics of an aerial manipulator interacting with flexible cantilever beams," *IEEE/ASME Transactions on Mechatronics*, 2022.

[3] A. Ollero, M. Tognon, A. Suarez, D. Lee, and A. Franchi, "Past, present, and future of aerial robotic manipulators," *IEEE Transactions on Robotics*, vol. 38, no. 1, pp. 626–645, 2021.

[4] K. Zhang, P. Chermprayong, F. Xiao, D. Tzoumanikas, B. Dams, S. Kay, B. B. Kocer, A. Burns, L. Orr, C. Choi *et al.*, "Aerial additive manufacturing with multiple autonomous robots," *Nature*, vol. 609, no. 7928, pp. 709–717, 2022.

[5] H. Hsiao, J. Sun, H. Zhang, and J. Zhao, "A mechanically intelligent and passive gripper for aerial perching and grasping," *IEEE/ASME Transactions on Mechatronics*, 2022.

[6] D. Brescianini and R. D'Andrea, "Computationally efficient trajectory generation for fully actuated multirotor vehicles," *IEEE Transactions on Robotics*, vol. 34, no. 3, pp. 555–571, 2018.

[7] S. Park, J. Lee, J. Ahn, M. Kim, J. Her, G.-H. Yang, and D. Lee, "Odar: Aerial manipulation platform enabling omnidirectional wrench generation," *IEEE/ASME Transactions on mechatronics*, vol. 23, no. 4, pp. 1907–1918, 2018.

[8] G. Michieletto, M. Ryll, and A. Franchi, "Fundamental actuation properties of multirotors: Force–moment decoupling and fail–safe robustness," *IEEE Transactions on Robotics*, vol. 34, no. 3, pp. 702–715, 2018.

[9] M. Ryll, G. Muscio, F. Pierri, E. Cataldi, G. Antonelli, F. Caccavale, D. Bicego, and A. Franchi, "6d interaction control with aerial robots: The flying end-effector paradigm," *The International Journal of Robotics Research*, vol. 38, no. 9, pp. 1045–1062, 2019.

[10] B. Li, L. Ma, D. Huang, and Y. Sun, "A flexibly assembled and maneuverable reconfigurable modular multi-rotor aerial vehicle," *IEEE/ASME Transactions on Mechatronics*, 2021.

[11] P. Zheng, X. Tan, B. B. Kocer, E. Yang, and M. Kovac, "Tiltdrone: A fully-actuated tilting quadrotor platform," *IEEE Robotics and Automation Letters*, vol. 5, no. 4, pp. 6845–6852, 2020.

[12] A. Sakaguchi and K. Yamamoto, "A novel quadrotor with a 3-axis deformable frame using tilting motions of parallel link modules without thrust loss," *IEEE Robotics and Automation Letters*, vol. 7, no. 4, pp. 9581–9588, 2022.

[13] M. Zhao, K. Okada, and M. Inaba, "Versatile articulated aerial robot dragon: Aerial manipulation and grasping by vectorable thrust control," *The International Journal of Robotics Research*, p. 02783649221112446, 2022.

[14] F. Ruiz Vincueria, B. C. Arrue Ullés, and A. Ollero Baturone, "Sophie: Soft and flexible aerial vehicle for physical interaction with the environment," *IEEE Robotics and Automation Letters, 7 (4), 11086-11093.*, 2022.

[15] H. Jia, S. Bai, R. Ding, J. Shu, Y. Deng, B. L. Khoo, and P. Chirarattananon, "A quadrotor with a passively reconfigurable airframe for hybrid terrestrial locomotion," *IEEE/ASME Transactions on Mechatronics*, pp. 1–11, 2022.

[16] N. Bucki, J. Tang, and M. W. Mueller, "Design and control of a midair-reconfigurable quadcopter using unactuated hinges," *IEEE Transactions on Robotics*, 2022.

[17] A. Fabris, E. Aucone, and S. Mintchev, "Crash 2 squash: An autonomous drone for the traversal of narrow passageways," *Advanced Intelligent Systems*, vol. 4, no. 11, p. 2200113, 2022.

[18] B. Mu and P. Chirarattananon, "Universal flying objects: Modular multirotor system for flight of rigid objects," *IEEE Transactions on Robotics*, vol. 36, no. 2, pp. 458–471, 2019.

[19] F. Schiano, P. M. Kornatowski, L. Cencetti, and D. Floreano, "Reconfigurable drone system for transportation of parcels with variable mass and size," *IEEE Robotics and Automation Letters*, vol. 7, no. 4, pp. 12 150–12 157, 2022.

[20] R. Oung and R. D'Andrea, "The distributed flight array," *Mechatronics*, vol. 21, no. 6, pp. 908–917, 2011.

[21] H.-N. Nguyen, S. Park, J. Park, and D. Lee, "A novel robotic platform for aerial manipulation using quadrotors as rotating thrust generators," *IEEE Transactions on Robotics*, vol. 34, no. 2, pp. 353–369, 2018.

[22] D. Saldana, B. Gabrich, G. Li, M. Yim, and V. Kumar, "Modquad: The flying modular structure that self-assembles in midair," in *2018 IEEE International Conference on Robotics and Automation (ICRA)*. IEEE, 2018, pp. 691–698.

[23] B. Gabrich, G. Li, and M. Yim, "Modquad-dof: A novel yaw actuation for modular quadrotors," in *2020 IEEE International Conference on Robotics and Automation (ICRA)*. IEEE, 2020, pp. 8267–8273.

[24] J. Xu, D. S. D'Antonio, and D. Saldaña, "H-modquad: Modular multi-rotors with 4, 5, and 6 controllable dof," in *2021 IEEE International Conference on Robotics and Automation (ICRA)*. IEEE, 2021, pp. 190–196.

[25] S. Bai and P. Chirarattananon, "Splitflyer air: A modular quadcopter that disassembles into two bicopters mid-air," *IEEE/ASME Transactions on Mechatronics*, pp. 1–10, 2022.

[26] R. Ding, Y.-H. Hsiao, H. Jia, S. Bai, and P. Chirarattananon, "Passive wall tracking for a rotorcraft with tilted and ducted propellers using proximity effects," *IEEE Robotics and Automation Letters*, vol. 7, no. 2, pp. 1581–1588, 2022.

[27] R. Mahony, V. Kumar, and P. Corke, "Multirotor aerial vehicles: Modeling, estimation, and control of quadrotor," *IEEE Robotics and Automation Magazine*, vol. 19, no. 3, pp. 20–32, 2012.

[28] D. Mellinger, N. Michael, and V. Kumar, "Trajectory generation and control for precise aggressive maneuvers with quadrotors," *The International Journal of Robotics Research*, vol. 31, no. 5, pp. 664–674, 2012.

[29] A. Nikou, G. C. Gavridis, and K. J. Kyriakopoulos, "Mechanical design, modelling and control of a novel aerial manipulator," in *2015 IEEE International Conference on Robotics and Automation (ICRA)*, 2015, pp. 4698–4703.

[30] Y. Chen, J. Liang, Y. Wu, Z. Miao, H. Zhang, and Y. Wang, "Adaptive sliding-mode disturbance observer-based finite-time control for unmanned aerial manipulator with prescribed performance," *IEEE Transactions on Cybernetics*, 2022.

Huaiyuan Jia received a B.S. degree in mechanical engineering from Shanghai Jiaotong University, Shanghai, China, in 2017. He was a research assistant with the Department of Automation, University of Science and Technology of China, in 2019. He is currently pursuing a Ph.D. degree at the Department of Biomedical Engineering, City University of Hong Kong.

Songnan Bai received a B.S. degree in mechanical engineering from Xi'an Jiaotong University, Xi'an, China, in 2017 and an M.S. degree in mechanical engineering from City University of Hong Kong, Hong Kong. He is currently pursuing a Ph.D. degree at the Department of Biomedical Engineering, City University of Hong Kong.

Pakpong Chirarattananon (S'12-M'15) received a B.A. degree in Natural Sciences from the University of Cambridge, U.K., in 2009 and a Ph.D. degree in Engineering Sciences from Harvard University, Cambridge, MA, USA, in 2014.

He is currently an Associate Professor at the Department of Biomedical Engineering, City University of Hong Kong, Kowloon, Hong Kong SAR, China. His research interests include bio-inspired robots, micro air vehicles, and the applications of control and dynamics in robotic systems.

SUPPLEMENTARY MATERIALS FOR

AERIAL MANIPULATION VIA MODULAR QUADROTORS WITH PASSIVELY FOLDABLE AIRFRAMES

Huaiyuan Jia, Songnan Bai, and Pakpong Chirarattananon

Department of Biomedical Engineering,
City University of Hong Kong,
Tat Chee Avenue, Hong Kong SAR, China.

S1. RELIABILITY TESTS OF THE DOCKING MECHANISM

To verify the reliability of the docking mechanism, drop tests were conducted to assess the effects of position misalignment and angular misalignment on docking success. The robot module with Part B of the mechanism was released from above onto the fixed base (Part A) with the robot turned off. The drop heights were between 5 cm to 10 cm.

For position misalignment, the robot was dropped 38 times with translation misalignments within 3 cm and minimal angular misalignment (less than 5°). The misalignment locations in the first quadrant is representative of the entire two-dimensional space due to the 4-fold rotational symmetry. Out of 38 tests, 26 resulted in successful docking, achieving a success rate of 100% for misalignments within 2 cm ($20/20$ attempts). Docking failures led to the robot falling off the base.

For angular misalignment, the position misalignment was minimized (less than 1 cm) while varying the yaw angle. The robot was dropped 15 times with yaw misalignments ranging from 0° to 45° to cover all possibilities (taking into consideration the symmetry). A 100% success rate was achieved for yaw misalignments under 25° ($9/9$ attempts); the success rate decreased to 67% when all cases are considered (10/15 attempts). In failed docking attempts, the robot remained on the base.

The drop test results verify that the docking mechanism is reliable for position and angular misalignments within certain ranges. The success rate decreases significantly for larger misalignments, indicating the need to improve docking reliability and tolerances in the future. By refining the design and control to better handle misalignments, the docking mechanism can be enhanced to expand the operational conditions

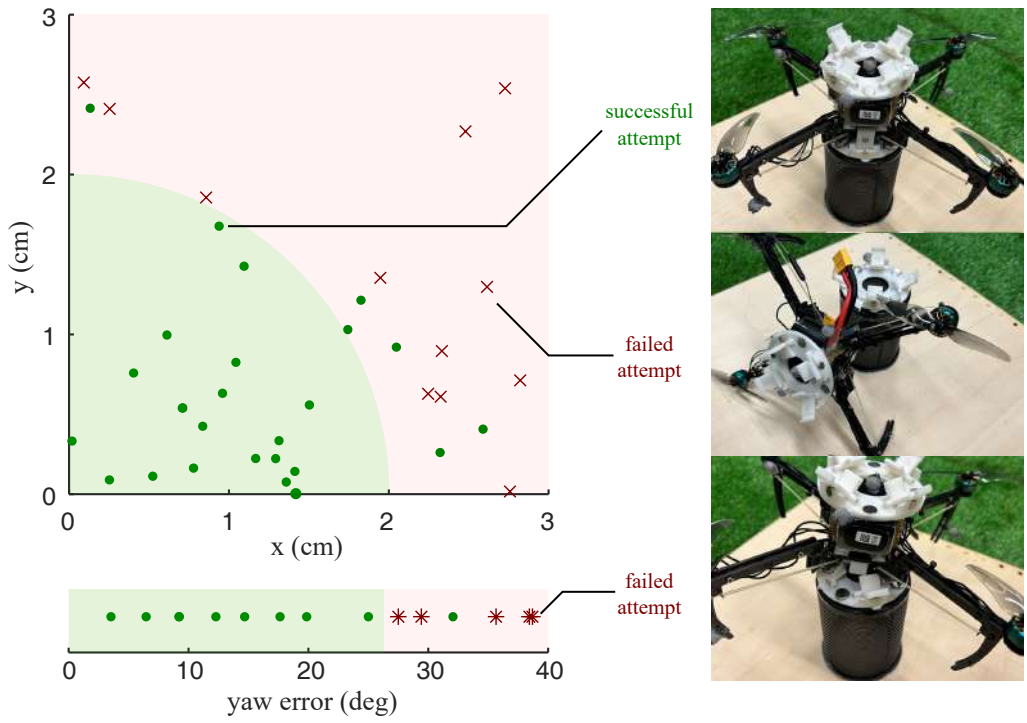

Fig. S1. Experiment results of the docking tests with: position errors (top) and angular errors (bottom). Photos of different docking results: a successful attempt (top); a failed attempt caused by a large position error (middle); and a failed attempt caused by a large yaw error (bottom).

S2. Maximum Tilt Angle Analysis

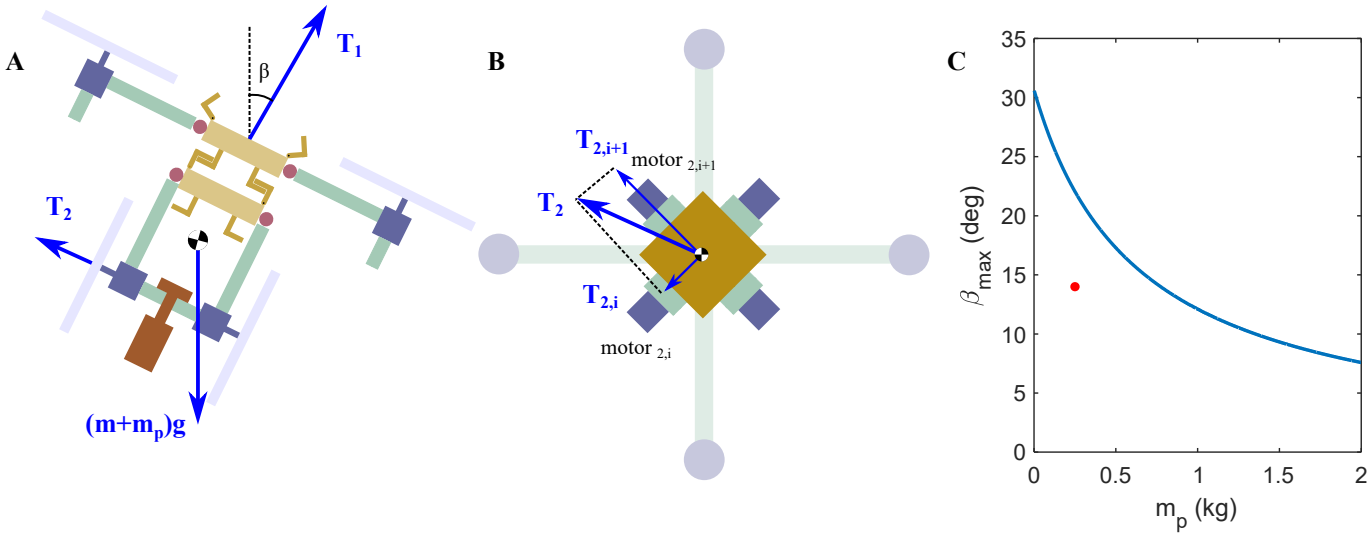

Fig. S2. (A) Diagram of a two-module multirotor carrying a payload, depicting the tilt angle β. The rotors on the folded arms produce horizontal force to induce the tilt. (B) View of the robot as seen from along the Z_B axis. The projected thrust vectors are shown. (C) Maximum tilt angle as limited by the payload mass according to (S3). The red dot denotes the tilt angle in the experiment (Section. IV.C).

We analyze a fully actuated multirotor composed of two quadrotor modules carrying a payload. Tilt while hovering is achieved by using the rotors on the folded arms to generate horizontal force. We simplify the model by assuming the top module's motors can always generate necessary thrust and torque, the lower module's joint angles are 90°, and position control is neglected. As shown in Figure S2A, the propulsive forces from the rotors on the folded and unfolded arms combine to generate thrust counteracting gravity and sustaining hovering: $\mathbf{T}_1 + \mathbf{T}_2 = -(m + m_p)g\mathbf{e}_3 = 0$, where $\mathbf{T}_i = \sum_{j=1}^{4} \mathbf{T}_{i,j}$ is the collective thrust of the i^{th} robot and $m + m_p$ is the total mass. The necessary force on the lower module is

$$T_2 = (m + m_p)g \sin\beta. \tag{S1}$$

As depicted in Fig. S2B, the force T_2 can be decomposed into two perpendicular elements: $T_{2,i}$ and $T_{2,i+1}$. For rotors located on the folded joints, the maximum force is limited by the elastic torque $\tau_e(\alpha = 90°)$ to avoid arm unfolding, so we have $T_{2,i} < \tau_e(\alpha = 90°)/l_a$. Thrust T_2 is maximized when the relative angle between T_2 and $T_{2,i}$ is 45°. As a result,

$$\max T_2 = \sqrt{2}\tau_e(\alpha = 90°)/l_a. \tag{S2}$$

Combining (S1) and (S2), we obtain the maximum tilt angle as

$$\max\beta = \arcsin\left(\frac{\sqrt{2}\tau_e(\alpha = 90°)}{(m + m_p)\, g l_a}\right), \tag{S3}$$

which decreases with increasing payload weight as shown in Fig. S2C. The limit for when m_p = 250 g is 22°, slightly higher than 14° demonstrated in the experiment. This is because the simplified calculation neglects the effort to control the attitude and position of the robot.

S3. Limits of Gripping Force and Payload Mass without Anchoring Mechanism

We seek to calculate (i) the gripping force of the rotor arms and (ii) the maximum weight of the payload that the robot can carry by gripping without the use of anchors or hooks. In such cases, the maximum weight that the robot can carry ($m_p g$) is limited by the friction caused by the grasp (normal force induced by the grippers). A diagram illustrating the gripping process is shown in Fig. S3. The gripping torque is dependent on the distance between the tips of the opposite arms. To simplify the analysis, we assume that the gripping configuration is symmetric such that the joint angles of all four arms are the same. During static gripping, the torque generated by the elastic components is balanced by the normal force N and friction force f at the contact point:

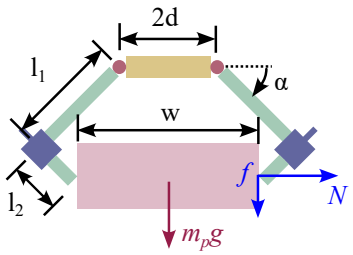

Fig. S3. A diagram showing the forces acting on a simple (rectangular prism) payload when the grasp is achieved with friction instead of anchoring. The link lengths are $l_1 = 65$ mm and $l_2 = 36$ mm. Note that only a two-dimensional section is shown.

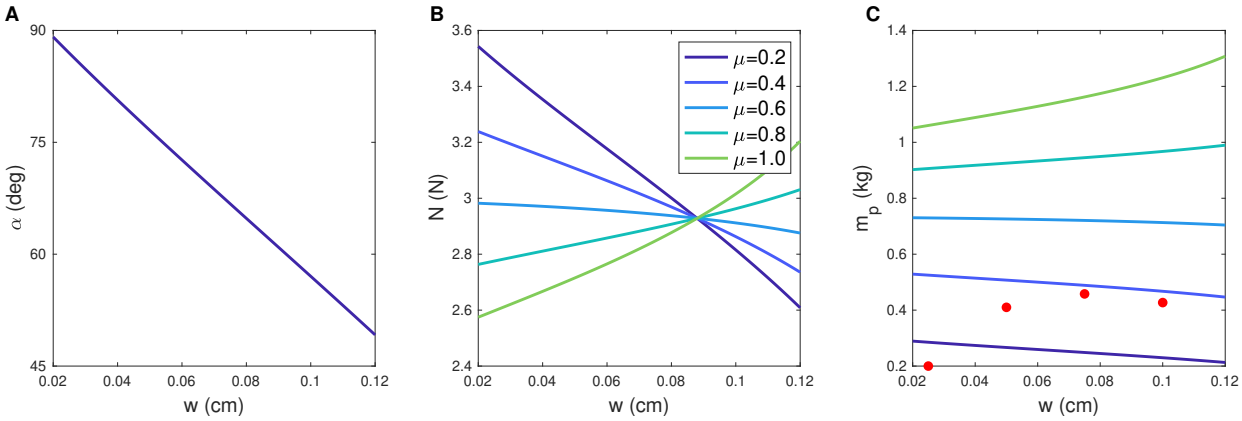

Fig. S4. (A) Joint angle as a function of the payload's width. (B) Maximum normal force predicted by (S6). (C) Maximum payload weight as limited by friction according to (S7).

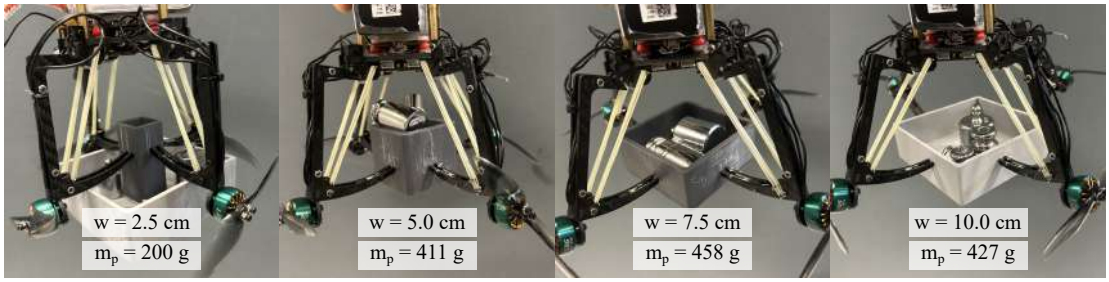

Fig. S5. The proposed robot grasped the payload with different container sizes (the maximal capacity of each container was tested by changing the weights inside the container).

$$\tau_e(\alpha) = N(l_1 \sin\alpha + l_2 \cos\alpha) - f(l_1 \cos\alpha - l_2 \sin\alpha), \tag{S4}$$

in which the elastic torque varies with the angle α as described by (2) and Fig. 2C. The angle is determined by the load's width w according to (see also Fig. S4A)

$$\alpha(w) = 2\arctan\left(\frac{\sqrt{l_2^2 + l_1^2 - (w/2 - d)^2} - l_2}{l_1 + w/2 - d}\right), \tag{S5}$$

allowing us to treat τ_e as a function of w instead of α. Next, since the maximum friction is proportional to the normal force via the coefficient μ: $f \leq \mu N$, (S6) is rewritten as:

$$N \leq \frac{\tau_e(w)}{(l_1 \sin(\alpha(w)) + l_2 \cos(\alpha(w))) - \mu(l_1 \cos(\alpha(w)) - l_2 \sin(\alpha(w)))}. \tag{S6}$$

This equation shows how the maximum gripping force varies with the friction coefficient μ and the width of the payload w. For the physical parameters listed in Table I, we yield the upper limit of N as a function of μ and w as presented in Fig. S4C. It can be seen that both the payload size w and the friction coefficient μ affect N, but the influence of μ is minimized at a particular w near 9 cm. This is when the term $l_1 \cos(\alpha(w)) - l_2 \sin(\alpha(w))$ in (S6) is zero.

Subsequently, the mass limit of the payload can be evaluated using the fact that $m_p g = 4f \leq 4\mu N$ (four symmetric arms). That is,

$$m_p \leq \frac{4\mu\tau_e(w)/g}{(l_1 \sin(\alpha(w)) + l_2 \cos(\alpha(w))) - \mu(l_1 \cos(\alpha(w)) - l_2 \sin(\alpha(w)))}, \tag{S7}$$

which is plotted in Fig. S4C. It demonstrates that the limit of m_p is largely dependent on μ. Relying on the friction alone (without leveraging the anchors) severely restricts the maximum payload mass when μ is low.

A. Empirical Validation

To verify the analysis of the gripping force, we 3D-printed containers with square cross-sections corresponding to $w = 2.5, 5.0, 7.5$, and 10.0 cm. The smooth finish of the resin (Grey Resin, Formlabs Form 3) results in a relatively low coefficient between the gripper and the payload.

We handheld the robot with the dummy payload grasped by four arms. Weights were added to the container to determine the upper limit of m_p for different payload sizes. The outcomes are shown in Figs. S4C (points) and S5. They show relatively low payload weights (< 0.5 kg) compared to the 1.4-kg load carried through the hooks in the flight experiment in Section IV-D, likely due to the low friction coefficient. We believe the abnormally low mass limit for $w = 2.5$ cm is due to the large joint angle ($alpha \approx 90^\circ$), which is near the joint limit. The outcomes demonstrate the advantage of the hook-like tips when deployed with a compatible payload.

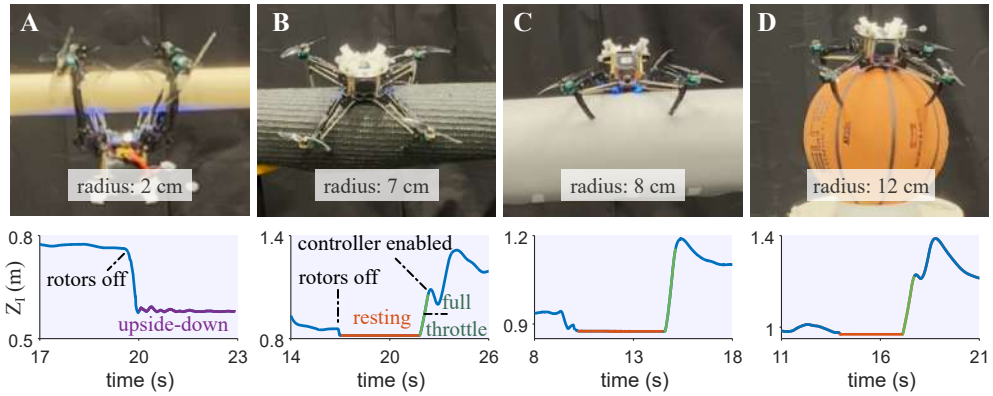

Fig. S6. Results of perching on different objects. The robot stayed stably on larger objects but failed to stabilize on the smallest tube and flipped upside down. (A) A cardboard tube with a radius of 2 cm. (B) A non-smooth tube with a radius of 7 cm. (C) A tube with a radius of 8 cm. (D) A basketball (radius: 12 cm).

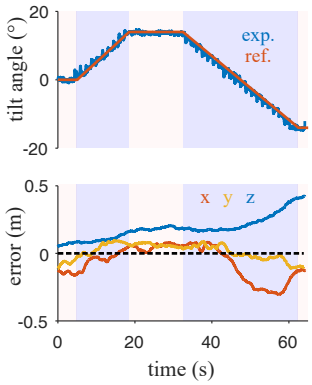

Fig. S7. Attitude and position tracking the performance of a fully-actuated multirotor composed of two modules with the integral term in the controller disabled. The RMSEs are $1.2°$ (tilt angle), and $[14, 6, 21]$ cm (position).

TABLE S1
COMPARISON OF RECONFIGURABILITY, MODULARITY, AND AERIAL MANIPULATION ABILITY

References	**Reconfigurable after construction**		**Modular**		**Thrust vectoring**	**Grasping or payload transport**
	Active	**Passive**	**Flight-capable subunit**	**Autonomous (dis)assembly**		
This work		✓	✓	✓	✓	✓
Li *et al.*, 2021 [10]	✓		✓	×	✓	×
Zhao *et al.*, 2022 [13]	✓		×	×	✓	✓
Sakaguchi *et al.*, 2022 [12]	✓		not modular		✓	✓
Zheng *et al.*, 2020 [11]	✓		not modular		✓	×
Bucki *et al.*, 2022 [16]		✓	not modular		✓	✓
Ruiz *et al.*, 2022 [14]		✓	not modular		×	✓
Saldana *et al.*, 2018 [22]	not reconfigurable		✓	✓	×	×
Bai *et al.*, 2022 [25]	not reconfigurable		✓	✓	×	×
Xu *et al.*, 2021 [24]	not reconfigurable		✓	×	✓	×
Mu *et al.*, 2019 [18]	not reconfigurable		×	×	×	✓
Schiano *et al.*, 2022 [19]	not reconfigurable		×	×	×	✓
Oung *et al.*, 2011 [20]	not reconfigurable		×	×	×	×